



# Determination of the material model and damage parameters of a carbon fiber reinforced laminated epoxy composite for high strain rate planar compression

Chen Shi<sup>a</sup>, Baoqiao Guo<sup>a,\*</sup>, Mustafa Sarıkaya<sup>b</sup>, Muhammet Çelik<sup>b</sup>, Pengwan Chen<sup>a</sup>, Mustafa Güden<sup>b</sup>

<sup>a</sup> State Key Laboratory of Explosion Science and Technology, Beijing Institute of Technology, Beijing, 100081, China

<sup>b</sup> Dynamic Testing and Modeling Laboratory and Department of Mechanical Engineering, Izmir Institute of Technology, Gülbahçe Köyü, Urla, Izmir, Turkey

## ARTICLE INFO

### Keywords:

Carbon fiber composite  
MAT\_162  
Progressive damage  
High strain rate  
Compression

## ABSTRACT

The progressive failure of a 0°/90° laminated carbon fiber reinforced epoxy composite was modeled in LS-DYNA using the MAT\_162 material model, including the strain rate, damage progression and anisotropy effects. In addition to conventional standard and non-standard tests, double-shear and Brazilian tests were applied to determine the through-thickness shear modulus and the through-thickness tensile strength of the composite, respectively. The modulus reduction and strain softening for shear and delamination parameters were calibrated by low velocity drop-weight impact tests. The rate sensitivities of the modulus and strength of in-plane and through-thickness direction were determined by the compression tests at quasi-static and high strain rates. The fidelity of the determined model parameters was finally verified in the in-plane and through-thickness direction by the 3D numerical models of the Split Hopkinson Pressure Bar compression tests. The numerical bar stresses and damage progressions modes showed acceptable correlations with those of the experiments in both directions. The composite failed both numerically and experimentally by the fiber buckling induced fiber-matrix axial splitting in the in-plane and the matrix shear fracture in the through-thickness direction.

## 1. Introduction

A common method of pre-testing aerospace components/structures made of carbon fiber reinforced polymer composites (CFRPCs) against dynamic loading such as bird strikes and debris and engine fragment impacts is the full-scale component test. As a part of certification process, although full-scale tests give realistic response against impact, they are too expensive to implement due to the need for the transportation of structures to testing facility and the use of large and heavy equipment and tools. Numerically validated full-scale tests decrease the number of tests; hence, reduce the cost and time in designing components with CFRPCs. The numerical models of full-scale tests however require successful material constitutive and damage parameters that can predict deformation and damage by taking into account the effects of fiber lay-up sequence and orientation for both unidirectional (UD) and plain weave (PW) laminates at varying strain rates. Despite the fact that CFRPCs have the highest rate of applications in aerospace industry among polymer matrix composites, the material constitutive and

damage parameters including the strain rate, damage progression and anisotropy effects are still missing in the literature. There have been various studies on modeling the damage formation in CFRPCs under impact loads, but these studies were mostly conducted for low velocity impact (LVI) delamination type damages. For example, Maio et al. [1] determined the material softening parameters of an IM7/8552 composite through LVI tests. Qu et al. [2] modeled the LVI of a TR50S15L carbon fiber/YPH-308 epoxy composite by combining virtual crack-closure technique and cohesive zone model. Farooq and Myler [3] modeled a carbon fiber reinforced composites subjected to the LVI of flat and round-end projectiles.

The present study was conducted to determine the material constitutive and damage parameters of a laminated (0°/90°) CFRPC through coupon level tests and to model its deformation response by including the effects of strain rate, damage progression and anisotropy. Various test methods and numerical calibrations were conducted to determine the material model parameters. The validity of the determined material model parameters was further verified with the Split Hopkinson

\* Corresponding author.

E-mail address: [baqiao\\_guo@bit.edu.cn](mailto:baqiao_guo@bit.edu.cn) (B. Guo).

<https://doi.org/10.1016/j.ijimpeng.2020.103771>

Received 6 April 2020; Received in revised form 24 July 2020; Accepted 8 November 2020

Available online 12 November 2020

0734-743X/© 2020 Elsevier Ltd. All rights reserved.

Pressure Bar (SHPB) tests in the in-plane and through-thickness directions. There are various composite material models for different purposes in the explicit FE program of LS-DYNA. For example, the MAT\_054 is generally used for the damage simulations of large structural orthotropic materials including UD tape laminates and requires the minimum number of input parameters. It uses the Chang-Chang failure criterion [4] beyond the elastic region to determine the failure of individual ply. The MAT\_058 is suitable for the plane and shell type problems in UD, laminate and woven fabric composites. The MAT\_162 is used to model the progressive failure in UD, laminate and PW composites [5]. Both, solid elements and 3D models are incorporated into the numerical model. Furthermore, the MAT\_162 successfully incorporates the effects of strain rate, damage progression and anisotropy in the progressive failure model of composites and therefore it was selected for the present study.

## 2. Composite material model

### 2.1. Material model description

The MAT\_162 model is based on the Hashin's composite failure [6] and the Matzenmiller's damage criterion [7] and it takes into account both the effect of strain softening after failure and strain rate in tension

**Table 1**  
MAT\_162 material model parameters.

Notation	LS-DYNA Notation	Parameter
$\rho$	$\rho$	Density
$E_a$	EA	Young's modulus (Longitudinal)
$E_b$	EB	Young's modulus (Long-transverse)
$E_c$	EC	Young's modulus (Through-Thickness)
$\nu_{ba}$	PRBA	Poisson's ratio BA
$\nu_{ca}$	PRCA	Poisson's ratio CA
$\nu_{cb}$	PRCB	Poisson's ratio CB
$G_{ab}, G_{bc}, G_{ca}$	GAB, GBC, GCA	Shear modulus
$S_{aT}$	SAT	Longitudinal tensile strength
$S_{aC}$	SAC	Longitudinal compressive strength
$S_{bT}$	SBT	Transverse tensile strength
$S_{bC}$	SBC	Transverse compressive strength
$S_{cT}$	SCT	Through-thickness tensile strength
$S_{FC}$	SFC	Crush strength
$S_{FS}$	SFS	Fiber shear strength
$S_{abo}, S_{bco}, S_{cao}$	SAB, SBC, SCA	Shear strength
$S_{FFC}$	SFFC	Scale factor for residual compressive strength
$\phi$	PHIC	Coulomb friction angle
$E\_LIMIT$	E\_LIMIT	Element eroding axial strain
$S$	S\_DELM	Scale factor for delamination criterion
$OMGMX$	OMGMX	Limit damage parameter for elastic modulus reduction
$ECRSH$	ECRSH	Limit compressive relative volume strain
$EEXPXN$	EEXPXN	Limit tensile relative volume strain
$C_{rate1}$	CERATE1 (C1)	Coefficient for strain rate dependent strength properties
$C_{rate2}$	CERATE2 (C2)	Coefficient for strain rate dependent axial modulus
$C_{rate3}$	CERATE3 (C3)	Coefficient for strain rate dependent shear modulus
$C_{rate4}$	CERATE4 (C4)	Coefficient for strain rate dependent transverse modulus
$m_1$	AM1	Strain softening for fiber damage in direction A
$m_2$	AM2	Strain softening for fiber damage in direction B
$m_3$	AM3	Strain softening for crush and punch shear damage
$m_4$	AM4	Strain softening for matrix and delamination damage

and shear. There are 35 parameters in this material model as tabulated in Table 1. In the same table,  $a$  and  $b$  refer to in-plane directions and  $c$  through-thickness direction. The strength and modulus parameters are determined directly from tests, while the damage parameters including the limit damage parameter for elastic modulus reduction (OMGMX) are determined by the numerical calibrations of tests. The MAT\_162 predicts 5 fiber and 2 matrix damage modes for a PW composite as tabulated in Table 2. These are the fill and warp direction fiber tension/shear, the fill and warp direction fiber compression, the fiber crush and in-plane and parallel matrix failure. The fiber tension/shear failure mode is

$$f_1 - r_7^2 = \left( \frac{E_a \langle \epsilon_a \rangle}{S_{aT}} \right)^2 + \left( \frac{G_{ac} \epsilon_{ca}}{S_{FS}} \right)^2 - r_7^2 = 0 \quad (1)$$

where,  $r_7$  is the damage threshold having a value of 1 without damage and its value is updated as damage is accumulated in the associated damage mode. Elastic moduli reduction ( $E'_i$ ) is expressed in terms of the associated damage parameter ( $\varpi_i$ ) as

$$E'_i = (1 - \varpi_i) E_i \quad (2)$$

and  $\varpi_i$  is

$$\varpi_i = \max \left\{ \dot{\varphi}_j q_{ij} \right\} = 1 - e^{-\left( \frac{1 - r_j}{m_j} \right)} \quad (3)$$

$E_i$  is the initial elastic modulus,  $r_j$  is the damage threshold computed from the associated damage function, and  $m_j$  is the material damage parameter. In Eq. (3),  $\dot{\varphi}_j$  is the scalar damage function which controls the amount of growth,  $q_{ij}$  ( $i = 1, 2, 4 \dots 6$  and  $j = 1, 2, 3, \dots 7$ ). The amount of growth provides the coupling between the individual damage variables ( $i$ ) and the various damage modes ( $j$ ) in Table 2. There are four material damage parameters ( $m_1, m_2, m_3$  and  $m_4$ ) to model the post elastic damage response of under different loading conditions. The tensile modulus reduction in-plane  $a$ -axis can be predicted by taking  $r_j = \frac{\epsilon_a}{\epsilon_{ay}}$  in Eq. (3) ( $\epsilon_a$  and  $\epsilon_{ay}$  are sequentially the strain and the failure strain corresponding to maximum stress in a tension test). The reduced elastic modulus ( $E'_a$ ) in  $a$  direction is

$$E'_a = e^{-\left[ \frac{1}{m_k} \left( 1 - \frac{\epsilon_k}{\epsilon_{ky}} \right)^{m_k} \right]} E_a \quad (4)$$

**Table 2**

Failure modes and failure criteria of MAT\_162 for PW composite [16].

Fiber failure modes	Failure criteria
Fiber tension-shear mode (mode 1f and 2f)	$f_7 - r_7^2 = \left( \frac{E_a \langle \epsilon_a \rangle}{S_{aT}} \right)^2 + \left( \frac{G_{ca} \epsilon_{ca}}{S_{aFS}} \right)^2 - r_7^2 = 0$ $f_8 - r_8^2 = \left( \frac{E_b \langle \epsilon_b \rangle}{S_{bT}} \right)^2 + \left( \frac{G_{cb} \epsilon_{cb}}{S_{bFS}} \right)^2 - r_8^2 = 0$
Compression fiber modes (mode 3f and 4f)	$f_9 - r_9^2 = \left( \frac{E_a \langle \epsilon_a \rangle}{S_{aC}} \right)^2 - r_9^2 = 0; \epsilon'_a = -\epsilon_a - \langle \epsilon_c \rangle \frac{E_c}{E_a}$ $f_{10} - r_{10}^2 = \left( \frac{E_b \langle \epsilon_b \rangle}{S_{bC}} \right)^2 - r_{10}^2 = 0; \epsilon'_b = -\epsilon_b - \langle \epsilon_b \rangle \frac{E_c}{E_b}$
Crush mode (mode 5f)	$f_{11} - r_{11}^2 = \left( \frac{E_c \langle -\epsilon_c \rangle}{S_{FC}} \right)^2 - r_{11}^2 = 0$
Matrix failure modes	Failure criteria
In-plane matrix mode (mode 6f)	$f_{12} - r_{12}^2 = \left( \frac{G_{ab} \epsilon_{ab}}{S_{ab}} \right)^2 - r_{12}^2 = 0$
Parallel matrix mode (delamination) (Mode 7f)	$f_{13} - r_{13}^2 = S^2 \left\{ \left( \frac{E_c \langle \epsilon_c \rangle}{S_{cT}} \right)^2 + \left( \frac{G_{bc} \epsilon_{bc}}{S_{bco} + S_{SRC}} \right)^2 + \left( \frac{G_{ca} \epsilon_{ca}}{S_{cao} + S_{SRC}} \right)^2 \right\} - r_{13}^2 = 0$

where,  $E_a$  is initial in-plane elastic modulus. The damage parameter  $m_1$  is predicted by fitting the following equation with experimental stress and strain ratios as

$$\frac{\sigma}{\sigma_y} = \frac{\varepsilon}{\varepsilon_{ay}} e^{\frac{1}{m_1} \left[ 1 - \left( \frac{\varepsilon}{\varepsilon_{ay}} \right)^{m_1} \right]} \quad (5)$$

where,  $\sigma$  and  $\sigma_y$  are the stress and the maximum stress, respectively.

The strain rate sensitivities of strength properties ( $S$ ) are formulated in the MAT\_162 as

$$\{S_{rt}\} = \{S_0\} \left( 1 + C_{rate1} \ln \frac{\dot{\varepsilon}}{\dot{\varepsilon}_0} \right) \quad (6)$$

$$\{S_{rt}\} = \begin{Bmatrix} S_{aT} \\ S_{aC} \\ S_{bT} \\ S_{bC} \\ S_{FC} \\ S_{FS} \end{Bmatrix} \text{ and } \{\dot{\varepsilon}\} = \begin{Bmatrix} \dot{\varepsilon}_a \\ \dot{\varepsilon}_a \\ \dot{\varepsilon}_b \\ \dot{\varepsilon}_b \\ \dot{\varepsilon}_c \\ \left( \dot{\varepsilon}_{ca}^2 + \dot{\varepsilon}_{bc}^2 \right)^{1/2} \end{Bmatrix} \quad (7)$$

And, the strain rate sensitivities of elastic modulus are

$$\{E_{rt}\} = \{E_0\} \left( 1 + \{C_{rate}\} \ln \frac{\dot{\varepsilon}}{\dot{\varepsilon}_0} \right) \quad (8)$$

$$\{E_{rt}\} = \begin{Bmatrix} E_a \\ E_b \\ E_c \\ G_{ab} \\ G_{bc} \\ G_{ca} \end{Bmatrix}, \{\dot{\varepsilon}\} = \begin{Bmatrix} \dot{\varepsilon}_a \\ \dot{\varepsilon}_b \\ \dot{\varepsilon}_c \\ \dot{\varepsilon}_{ab} \\ \dot{\varepsilon}_{bc} \\ \dot{\varepsilon}_{ca} \end{Bmatrix} \text{ and } \{C_{rate}\} = \begin{Bmatrix} C_{rate2} \\ C_{rate2} \\ C_{rate4} \\ C_{rate3} \\ C_{rate3} \\ C_{rate3} \end{Bmatrix} \quad (9)$$

where  $rt$  and  $o$  refer to the property,  $\dot{\varepsilon}$  is the strain rate and  $\dot{\varepsilon}_0$  is the reference strain rate.  $C_{rate1}$  is the strain rate constant for strength properties. Only one strain rate sensitivity  $C_{rate1}$  is used for all strength properties in the Mat\_162.  $C_{rate2}$ ,  $C_{rate3}$  and  $C_{rate4}$  are sequentially the strain rate constant for elastic modulus in  $a$ -axis, the strain rate constant for shear modulus and the strain rate constant for elastic modulus in  $c$ -axis.

## 2.2. A review of the material model parameter calibration studies

Xiao et al. [8] used a punch-shear-test to calibrate  $m_1$ ,  $m_2$ ,  $m_3$  and  $m_4$ , and  $EEXP$  (Limit tensile relative volume strain) of a PW S2-Glass/SC-15 epoxy composite. The initial load-drop in the load-displacement curve of a punch-shear-test corresponded to the initiation of a delamination type damage. The value of  $m_4$  was therefore calibrated with the detected initial load-drop and the value of  $m_3$  (softening due to punch shear) was calibrated with the experimental loads between the initial load-drop and maximum load. The value of  $m_1$  and  $m_2$  and  $EEXP$  were calibrated with the experimental loads after the maximum load corresponding to the fiber tensile/shear failure. A similar procedure was also used in the present work to calibrate the values of  $m_3$  and  $m_4$  as elaborated in Section 5. Deka et al. [9] projectile impact tested an E-Glass/PP composite. The softening parameters were then calibrated by varying the softening parameters of projectile impact test models until the numerical energy absorption and damage modes were matched with those of tests. The delamination factor  $S$  was optimized iteratively by matching the

numerical and experimental delaminated areas of the impacted plates in the through-thickness direction. Gama and Gillespie et al. [10] calibrated the strain rate dependent strength and modulus parameters and  $EEXP$  of a PW S2-Glass/SC-15 composite by the projectile impact tests. The residual velocities of the impact test models at different projectile impact velocities were matched with those of the impact tests by varying the strain rate parameters. Jordan et al. [11] calibrated the modulus reduction parameter  $OMGMX$  of an E-Glass/phenolic composite by the LVI tests and the limits of compressive volume strain for element eroding, the element eroding axial strain,  $E_{LIMT}$ ,  $EEXP$  and  $ECRSH$  by the ballistic impact tests. Taşdemirci et al. [12] determined the strain rate dependent strength and modulus parameters of an E-Glass fiber woven fabric reinforced polyester matrix composite by the compression tests at quasi-static and dynamic strain rates. Odaci [13] investigated the MAT\_162 material parameters of a PW glass fiber/polyester composite. The strength and modulus strain rate parameters were determined by the quasi-static and dynamic strain rate compression test, the modulus reduction parameter  $OMGMX$  by the LVI tests and  $E_{LIMT}$  and  $EEXP$  by the projectile impact tests. Hazzard et al. [14] modeled the buckling and depth of penetration of a cross-ply unidirectional Dyneema® polyurethane composite using a homogenized model. Molitor et al. [15] investigated the effect of punch shear and laterally constrained tests on the values of  $m_4$  softening parameter of an IM7/8552 composite and recommended the use of punch shear test for the determination of the limits of crush and fiber strength. Materials Sciences Corporation (MSC) and the University of Delaware Center for Composite Materials have recently proposed a testing methodology for obtaining the MAT\_162 material parameters [16]. The methodology is composed of both the standard and non-standard tests.

## 3. Materials and test methods

As-received composite plates ( $500 \times 500 \times 10$  mm) were made of  $0^\circ/90^\circ$  80 plies of Toray T300B carbon fiber reinforced/FRD-YG Epoxy composite. The composite is transversely isotropic in the in-plane direction,  $a$  and  $b$ . The tests methods and test specimens used to determine the MAT\_162 material model parameters are tabulated in Table 3 with the numbers from 1 to 7. The quasi-static strain rate tests were performed at  $1 \times 10^{-3} \text{ s}^{-1}$  in a Shimadzu AG-I universal test machine equipped with a video extensometer.

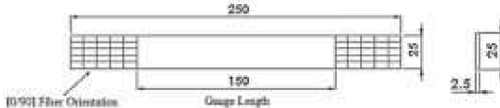
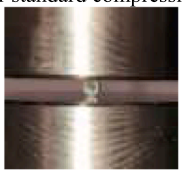
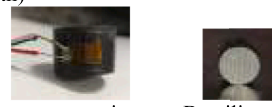
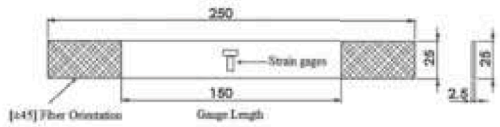
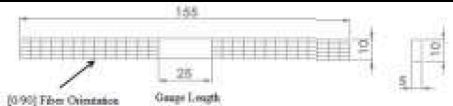
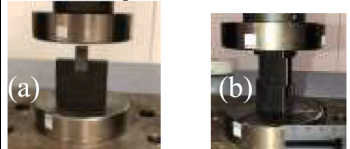

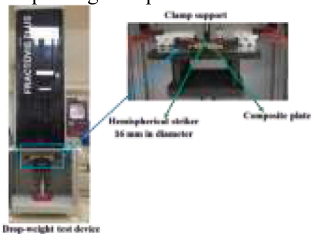
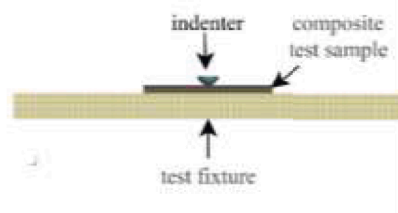
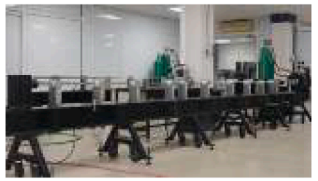

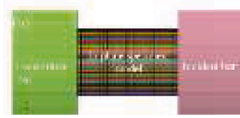
The in-plane elastic modulus ( $E_a$ ), tensile strength ( $S_{aT}$ ) and Poisson's ratio ( $\nu_{ba}$ ) were determined by tensile testing longitudinally and transversely strain-gaged end-tapped three test coupons ( $5 \times 25 \times 250$  mm in size) in accord with the ASTM D3039/D3039M 8 (Table 3, 1). The through-thickness elastic modulus ( $E_c$ ) and Poisons' ratios ( $\nu_{cb}$  and  $\nu_{ca}$ ) were determined by compression testing strain-gaged three cylindrical test specimens (20 mm in diameter and 15 mm in length) at the quasi-static strain rate (Table 3, 2). The through-thickness tensile strength ( $S_{cT}$ ) was determined by the Brazilian tests on three cylindrical test specimens (6.6 mm in diameter and 5 mm in length) core-drilled through-thickness direction of the as-received composite plates (Table 3, 2). In the Brazilian test, a central crack normal to the fiber plane formed after the test and the tensile strength ( $S_{cT}$ ) was then calculated using the following relation

$$S_{cT} = \frac{2P_{max}}{\pi DL} \quad (10)$$

where,  $P_{max}$ ,  $D$  and  $L$  are sequentially the maximum load and the diameter and length (thickness) of specimen.

The in-plane shear modulus ( $G_{ab}$ ) and matrix shear strength ( $S_{abo}$ ) were determined by the tensile tests on  $\pm 45^\circ$  ply oriented three composite coupons ( $5 \times 25 \times 250$  mm in size) in accord with the ASTM D 3518 (Table 3, 3). The in-plane compressive strength ( $S_{ac}$ ) was determined using the Illinois Institute of Technology Research Institute (IITRI) compression test fixture and end-tapped four compression test

**Table 3**  
The test methods and, test specimens used to determine. MAT\_162 material model parameters.

Parameter	Test method/Device/Fixture	Specimen/model
1 $E_a, E_b, \nu_{ba}$ , $S_{aT}, S_{bT}$ (a and b)	ASTM D3039/D3039M “Standard Test Method for Tensile Properties of Polymer Matrix Composite Materials”	 Tensile test specimen with strain gages
2 $E_c, \nu_{ca}, \nu_{cb}$ , $S_{cT}$	Non-standard compression and Brazilian tests 	Compression (20 mm in diameter and 15 mm in length) and Brazilian tests (6.6 mm in diameter and 5 mm in length)  Compression test specimen    Brazilian test specimen
3 $G_{ab}, G_{bc}, G_{ca}$ $S_{abo}, S_{bco}, S_{cao}$ (a, b, c ± 45° and through thickness)	ASTM D 3518 “Standard Test Method for In-plane Shear Response of Polymer Matrix Composite Materials by Tensile Test of a Laminate”	 In-plane shear test specimen
4 $S_{aC}$ , $S_{bC}$ (0° and 90°)	ASTM D3410 “Standard Test Method for Compressive Properties of Polymer Matrix Composite Materials with Unsupported Gage Section by Shear Loading” and IITRI compression test fixture.	 Compression test specimen
5 $S_{FC}, S_{FS}$ (through-thickness)	(a) Non-standard laterally constraint compression test and (b) Non-standard double-shear-test/Universal tension-compression test machine  Lateral constraint and double-shear-test fixtures	(a) 12.7 mm x 12.7 mm x 12.7 mm cubic specimen (b) Double-shear-test 4 in diameter and 20 mm in length  Double-shear-test specimen
6 $OMGMX$ $m1-m4$	ASTM D7136 “Standard Test Method for Measuring the Damage Resistance of a Fiber-Reinforced Polymer Matrix Composite to a Drop-Weight Impact”  Drop-weight impact test (LVI)	100x150 mm through-thickness plates  Drop-weight impact test model (LVI)
7 $C_{rate1}$ , $C_{rate2}$ , $C_{rate3}$ , $C_{rate4}$ , $m_1$ , $m_2$	Non-standard quasi-static and Split Hopkinson Pressure Bar (SHPB) compression tests and models  Compression SHPB	Compression test specimens 6.5 mm in diameter and length diameter; L/D=1 through a, b and c direction.  Core drilled compression tests specimens and end-caps  SHPB model



coupons ( $5 \times 10 \times 155$  mm in size) with the gage length of 25 mm in accord with the ASTM D3410 (Table 3, 4). The fiber crushing strength ( $S_{FC}$ ) and fiber shear strength ( $S_{FS}$ ) were determined using the laterally-constraint-compression and double-shear-test fixtures. In the laterally-constraint-compression test,  $S_{FS}$  was calculated using the flowing relation after the determination of  $S_{FC}$ ,

$$S_{FS} = 0.5S_{FC}\sin(2\theta) \quad (11)$$

where,  $\theta$  is the angle between the loading axis and fracture surface. The cubic composite specimens ( $12.7 \times 12.7 \times 12.7$  mm) were tested in the laterally-constraint-compression tool-steel test fixture (Table 3, 5(a)). In these tests, the cubic composite specimens constrained in the in-plane direction were compressed in the through-thickness direction by a square-cross-section tool steel punch. After the tests, the angle between the fiber crush plane and loading axis was determined using an image program.  $S_{FS}$  was also determined by the double-shear-test (Table 3, 5 (b)). The shear forces (double force) were applied to the normal to the in-plane direction of a cylindrical composite test specimen, 4 mm in diameter and 20 mm in length (Table 3, 5).

In addition, low velocity drop-weight tests were performed on  $5 \times 100 \times 150$  mm standard size composite test plates in the through-thickness direction in a CEAST drop-tower in accord with the ASTM D7136 (Table 3, 6). These tests were for the calibrations of OGMGX and softening parameters. The tests were performed using a standard 16 mm-diameter hemispherical impactor at an impact energy of 40 J at  $3.8 \text{ m s}^{-1}$  with a total weight of 5.48 kg.

The strain rate coefficient of strength ( $C_{rate1}$ ), axial modulus ( $C_{rate2}$ ), shear modulus ( $C_{rate4}$ ) and transverse modulus ( $C_{rate4}$ ) were determined by the compression tests at quasi-static and dynamic strain rates on the core-drilled, cylindrical compression test specimens, 6.6 mm in diameter and 10 mm in length, in the in-plane and through-thickness directions (Table 3, 7). The quasi-static tests were performed at  $10^{-3}$ ,  $10^{-2}$  and  $10^{-1} \text{ s}^{-1}$ , while the dynamic tests were performed using a compression SHPB at about 200 and  $600 \text{ s}^{-1}$ . The recent reviews on the assessments of the SHPB test are found in [17,18]. The SHPB stress ( $\sigma_s$ ), strain ( $\epsilon_s$ ) and strain rate ( $\dot{\epsilon}$ ) were calculated using the one dimensional elastic stress wave propagation in long bars as [19]

$$\sigma_s = \frac{A_b}{A_s} E_b \epsilon_T(t) \quad (12)$$

$$\epsilon_s = \frac{-2C_b}{L_s} \int_0^t \epsilon_R(t) dt \quad (13)$$

$$\dot{\epsilon} = \frac{-2C_b}{L_s} \epsilon_R(t) \quad (14)$$

where,  $t$ ,  $\epsilon_I$ ,  $\epsilon_R$ ,  $\epsilon_T$ ,  $L_s$ ,  $A_b$ ,  $A_s$  and  $E_b$  are sequentially the time, the incident, reflected and transmitted strains, the initial length of the specimen, the cross-sectional area of the bar and specimen and the elastic modulus of the bar. The used SHPB apparatus consisted of Inconel 718 bars, 500 mm striker, 3116 mm incident and 2050 mm transmitter bars, all with a diameter of 19.4 mm. A full-bridge strain gage was used to measure the strains on the Inconel bars. The elastic modulus and the density of the bar material were 204 GPa and  $7810 \text{ kg m}^{-3}$ , respectively. A high-speed camera at 20,000 fps was used to record the SHPB tests in order to observe the deformation modes of composite specimens in all principal directions. One of the assumptions made in the SHPB calculations is the force equilibrium between incident and transmitter bar [20,21]. In SHPB testing of brittle materials, specimen may fracture within the initially steeply-rising part of the incident stress at a time earlier than the time needed for the specimen to establish stress equilibrium. For this reason, the time to fracture should be at least 3 times the specimen's transit time (specimen length/specimen elastic wave velocity) [20]. Although, pulse shaping is a widely used method for

inducing a gradually rising incident wave, it was used in the present study to impose a lower strain rate on the specimen. An aluminum 1100 sheet in  $10 \times 10 \times 1$  mm size was placed at the end of incident bar of the SHPB. The sheet was attached to the end of the bar by applying a thin layer of grease. The plastic deformation of the sheet after the impact of striker bar induced a gradually rising incident stress; hence, a lower strain rate on composite test specimen.

#### 4. Modeling

In the in-plane and through-thickness SHPB compression test models, the incident and transmitted bars were modeled using eight-node constant stress solid elements. Since the experimental incident stress-wave was used as an input onto the incident bar in order to simulate the response of the composite more realistically, the striker bar model was excluded in the analysis. The bars were modeled using MAT01\_ELASTIC material model ( $\rho=7850 \text{ kg m}^{-3}$ ,  $E=204 \text{ GPa}$  and  $\nu=0.33$ ). Total 5mm-long 52,780 elements were used to simulate the bars, which provided 12 elements across the bar diameter and 140 elements along the bar length. The models of in-plane and through-thickness specimens are shown in Fig. 1(a) and (b), respectively. The composite specimen was modeled with 52 and 80 plies for the in-plane and through-thickness direction, respectively. The contacts between the specimen and incident and transmit bars were defined by the contact card of AUTOMATIC\_SURFACE\_TO\_SURFACE. The contacts between the composite plies were defined by ERODING\_SINGLE\_SURFACE contact algorithm. The reflected and transmitted stresses of the SHPB model were determined at the same locations with the strain gages on the bars in the experiments.

The same specimen sizes, impact energy and impact velocity were used in the LVI simulations of the composite in the through-thickness direction. The upper and lateral views of the LVI specimen were shown in Fig. 2(a) and (b). The density of the indenter in the model was increased until it gave a total weight of 5.48 kg as similar with the tests. The indenter, composite plate and test fixture were modeled using 14,336, 921,600 and 102,128 solid elements, respectively. An AUTOMATIC\_SINGLE\_SURFACE contact was defined between the plies of the composite. The contact between the composite test specimen and the test fixture was defined by the AUTOMATIC\_SURFACE\_TO\_SURFACE

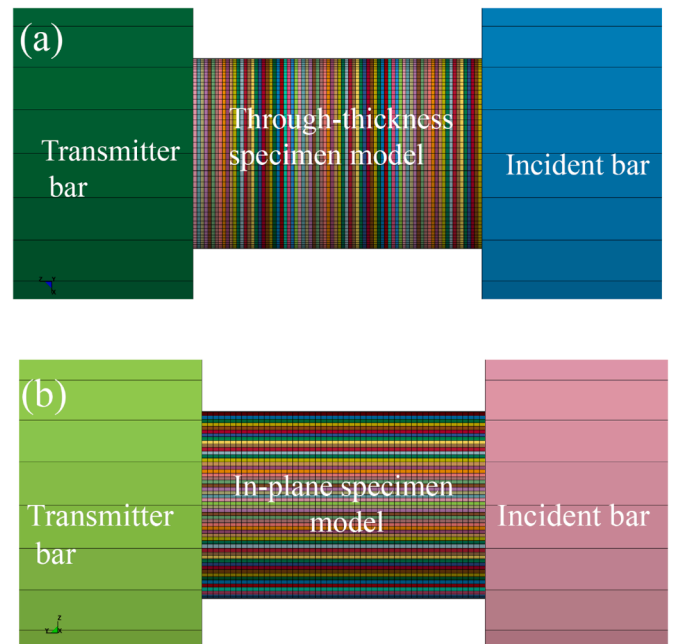


Fig. 1. Numerical model of SHPB test and specimen.

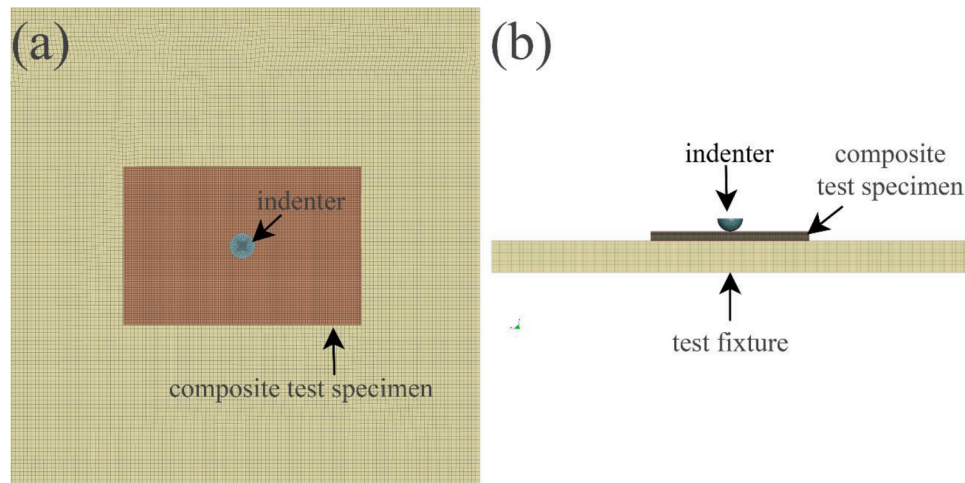


Fig. 2. Numerical model of LVI test.

contact algorithm, while an ERODING\_SURFACE\_TO\_SURFACE contact algorithm was used for the penetration condition. The static and dynamic coefficient of friction were 0.3 and 0.2, respectively.

## 5. Results and discussion

### 5.1. Quasi-static model parameters

Fig. 3(a) and (b) show the in-plane tensile and compressive stress-strain curves and the determined tensile and compression material model parameters, respectively. The average in-plane tensile elastic modulus, tensile strength and Poisson's ratio are sequentially 65.1 GPa, 736 MPa, and 0.03. The tensile failure of the composite in the in-plane direction occurs by fiber crushing and fiber-matrix separation/splitting as depicted in the inset of Fig. 3(a). The compression tests using the ITTRI test fixture (based on ASTM D3410); however, result in lower elastic modulus as compared with the tensile tests. The compression tests also exhibit large variations in the compressive strengths as seen in Fig. 3(b). An average compressive strength of 438.5 MPa was determined from these tests. The compressive stress-strain curves of small size test specimens used for the determination of the in-plane strain rate sensitivity parameters of modulus and strength show more consistent strength values between the tests and similar average compressive strength with ITTRI test fixture, but the moduli of these specimens are comparably lower, most likely due to the non-standard specimen sizes used in these tests. The dominant compressive failure modes in the in-plane direction are the fiber buckling and matrix-fiber axial splitting (Fig. 3(b)). Fig. 4(a) and (b) show sequentially the in-plane shear stress-strain curves and the through-thickness compression stress-strain and Poisson's ratio-strain curves, respectively. In the in-plane shear tests, the average in-plane shear modulus and shear strength (0.05 strain) are determined 3.61 GPa and 55 MPa (Fig. 4(a)), respectively. The failure mode in these tests is dominantly shear, while the delamination of plies is also seen at larger strains (Fig. 4(a)). The compression testing of 20 mm-diameter cylindrical specimens in the through-thickness direction using transversely strain-gaged specimens (placed in  $a$ - or  $b$ -direction) results in an average Poisson's ratio of 0.054 as seen in Fig. 4(b). Fig. 5(a) and (b) show the through-thickness double-shear-test stress-strain and Brazilian test tensile stress-displacement curves, respectively. The double-shear-tests (two tests) in the transverse direction result in an average through-thickness shear modulus of 5.5 GPa and an average fiber shear strength of 497 MPa (Fig. 5(a)). The deformation mode in double-shear-test is the shear of plies in the through-thickness direction as depicted in Fig. 5(a). The Brazilian through-thickness tensile tests result in an average through-thickness tensile

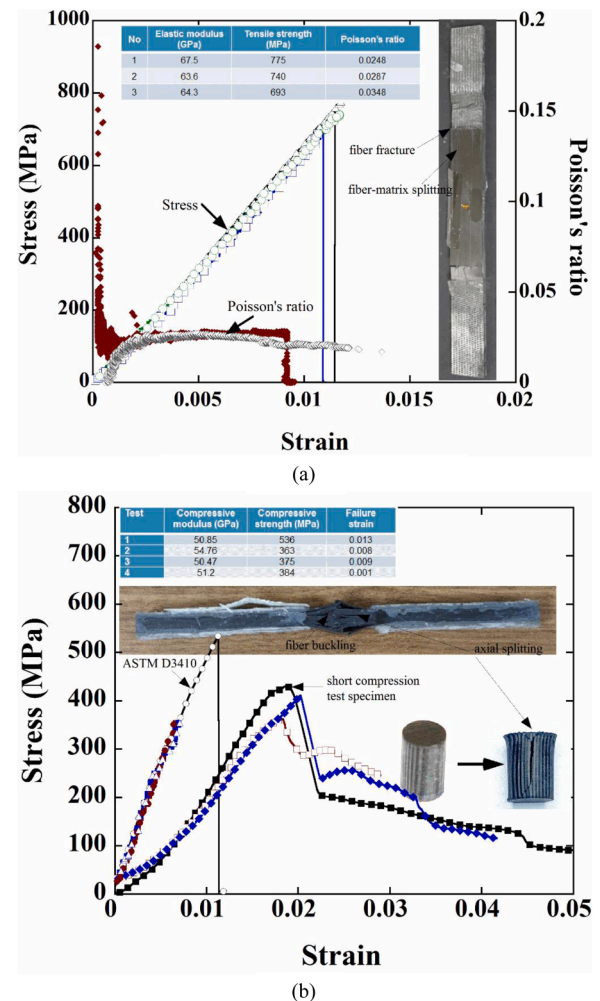


Fig. 3. In-plane (a) tensile stress-strain curves of three tests and tensile properties and (b) compression stress-strain curves of three tests and compression properties.

strength of 45 MPa (Fig. 5(b)). The failure mode in these tests is the axial matrix cracking parallel to loading axis as seen in Fig. 5(b). Fig. 6 shows the typical stress-displacement curve of a fiber crush test. The composite specimen in this test fails by the shear fracture through the fiber plane,

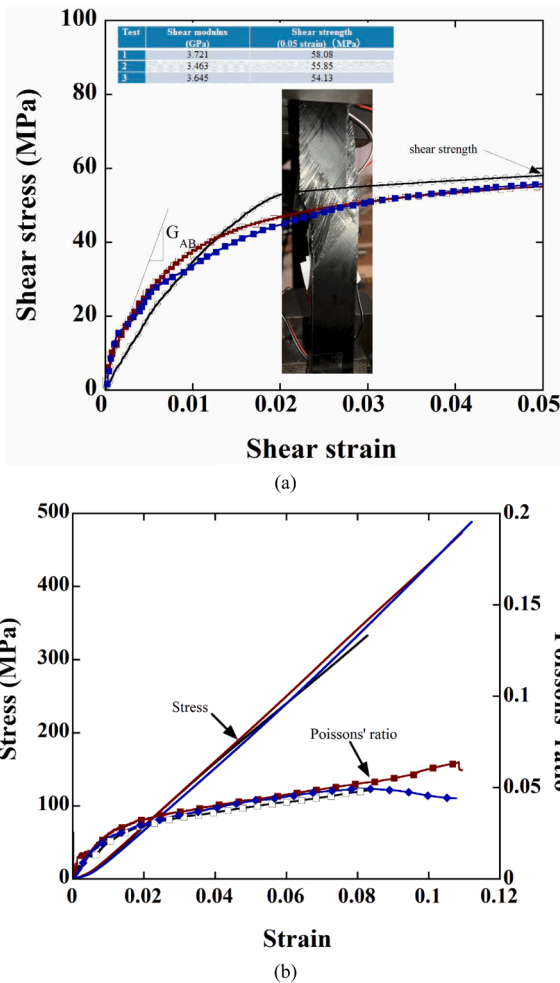


Fig. 4. In-plane (a) shear stress-shear strain curves and (b) Poissons' ratio.

making an angle of 48.4° with the fiber plane as shown in the inset of Fig. 6. The fiber crush strength is determined 1000 MPa, which gives a fiber shear strength of 497 MPa using Eq. (11). The fiber crush test is noted to result in a fiber shear strength the same as the double-shear-test as shown in Fig. 5(a).

5.2. Rate sensitivity parameter determination

Fig. 7(a-c) show sequentially the SHPB bar stresses with and without pulse shaper and the corresponding stress-strain and strain rate-strain curves of the specimens tested in the in-plane direction. The test using an aluminum pulse shaper, as noted in Fig. 7(a) and (c), has a more gradually increasing incident bar stress and results in lower specimen strain rates as compared with the test without pulse shaper. The average strain rate corresponding to the fracture stress or maximum stress was taken as the strain rate for the test (shown by dotted lines in Fig. 7(b) and (c)). By using this method, an average strain rate of ~200 s<sup>-1</sup> and ~600 s<sup>-1</sup> was determined for the tests with and without pulse shaper in the in-plane direction as shown in Fig. 7(c). The tests were also performed in the through-thickness direction at the same SHPB velocity with and without pulse shaper and the corresponding strain rates were determined 400 and 600 s<sup>-1</sup>, respectively.

Fig. 8(a) and (b) show the typical in-plane and through-thickness direction compression stress-strain curves at increasing strain rates, respectively. As seen in the same figures, the composite in both directions deforms elastically till fracture at quasi-static and high strain rates. The through-thickness direction however shows much higher fracture stresses and failure strains than the in-plane direction. The

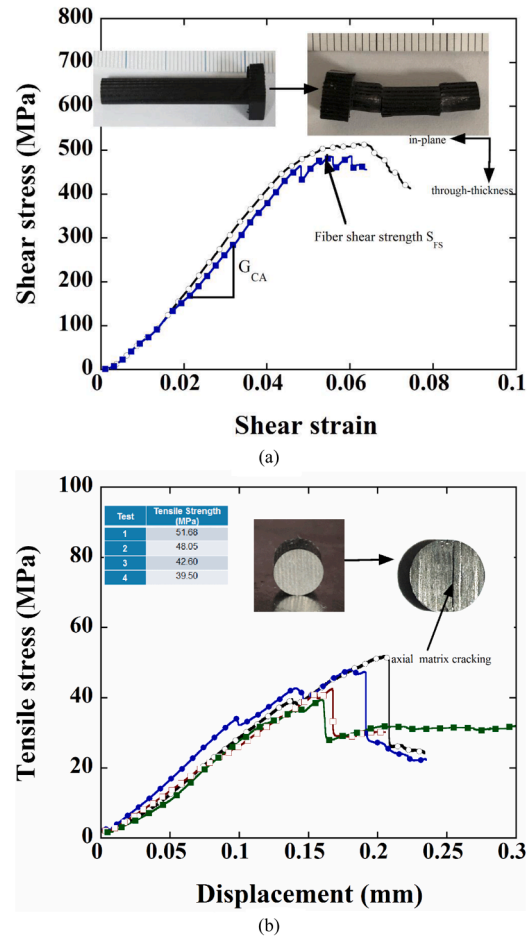


Fig. 5. Through-thickness (a) double-shear test shear stress-strain curves and (b) Brazilian test tensile stress-displacement curves.

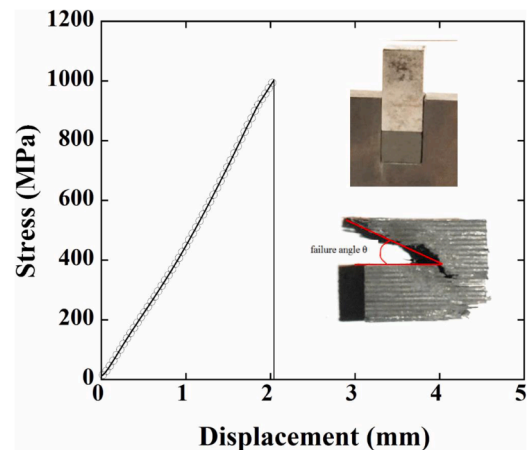


Fig. 6. The stress-displacement curve of a fiber crush test.

compressive strength increases with increasing strain rate in the in-plane direction as seen in Fig. 8(a). But, the compressive strength decreases as the strain rate increases in the through-thickness direction (Fig. 8(b)). The primary failure modes in the in-plane and through-thickness directions at quasi-static and high strain rates are the axial splitting (Fig. 8 (a)) and matrix dominated shear failure (Fig. 8(b)), respectively. Within the studies strain rate interval, almost no effect of strain rate on the composite failure modes is found.

The in-plane direction average compression strength increases from



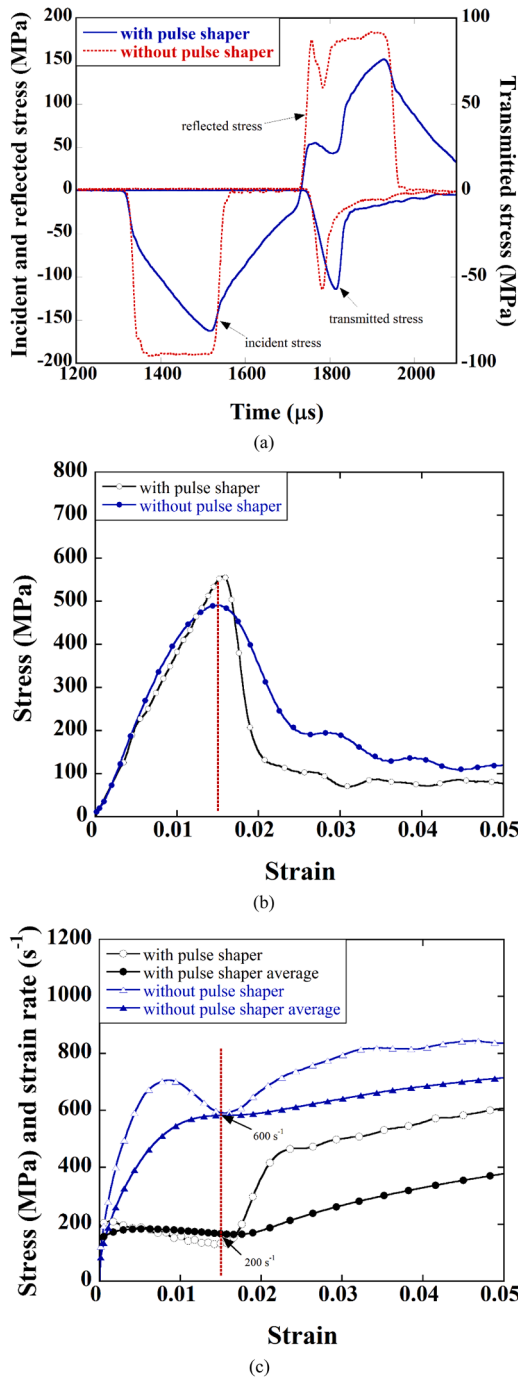


Fig. 7. (a) the bar stresses of the in-plane specimen in the SHPB compression test with and without pulse shaper and the corresponding (b) stress-strain and (c) strain rate and average strain rate-strain curves.

401.07 MPa to 534.78 MPa when the strain rate increases from  $10^{-3} \text{ s}^{-1}$  to  $600 \text{ s}^{-1}$  (Fig. 9(a)). While the through-thickness direction average compression strength decreases from 1068.71 MPa to 883.14 MPa when the strain rate increases from  $10^{-3} \text{ s}^{-1}$  to  $600 \text{ s}^{-1}$  (Fig. 9(b)). The average elastic modulus increases from 28.15 GPa at  $10^{-3} \text{ s}^{-1}$  to 40.09 GPa at  $600 \text{ s}^{-1}$  for the specimens tested in the in-plane direction and decreases from 9.17 GPa at  $10^{-3} \text{ s}^{-1}$  to 8.51 GPa at  $600 \text{ s}^{-1}$  for the specimens tested in the through-thickness. The results show that the composite has the strain rate dependent elastic modulus and fracture strength in the in-plane direction with a strain rate sensitivity parameter of  $\sim 0.03$  and has no strain rate dependent elastic modulus and fracture strength in the through-thickness direction.

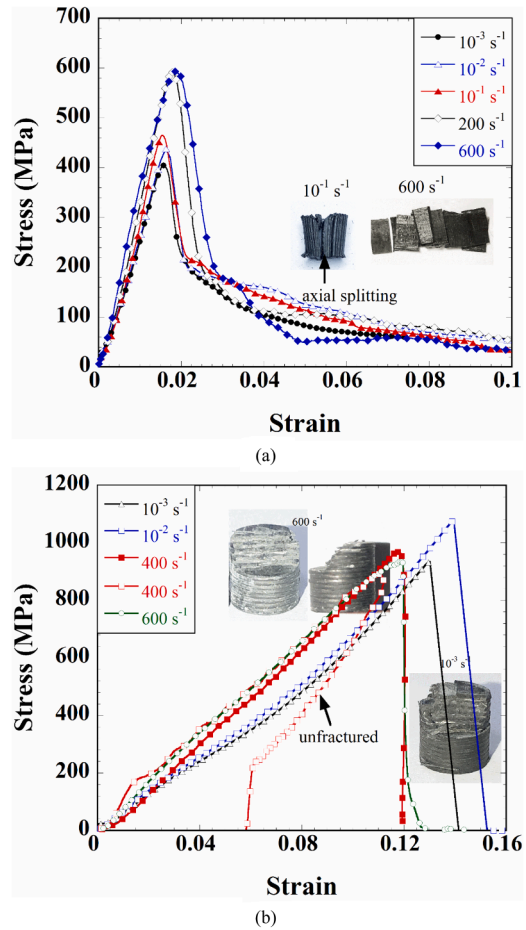


Fig. 8. Representative compression-stress strain curves at different strain rates (a) in-plane and (b) through-thickness direction.

There have been numerous experimental studies on the dynamic deformation behavior of UD and PW CFRPCs in the literature [22–31]. Houser et al. [31] investigated the static and high strain rate compression behavior of a 4518 woven carbon epoxy (SC-15) composite in the in-plane and through-thickness direction. The through-thickness and in-plane elastic modulus increased with increasing strain rate. Naik and Kavala [32] investigated the high strain rate compression behavior of a PW carbon/epoxy composite in the strain rate range  $680\text{--}2890 \text{ s}^{-1}$ . Although, the compressive strength in the through-thickness direction increased with increasing strain rate, no significant effect of strain rate was reported on the compressive strength in the in-plane direction. Chen et al. [27] tested a carbon fiber reinforced epoxy resin matrix composite at high strain rates in the in-plane direction. The failure strength and failure strain increased with increasing strain rate. Lu et al. [28] studied the in-plane mechanical properties of a carbon fiber PW composite at different strain rates. The results indicated that the in-plane mechanical properties and failure patterns were strain rate sensitive. At the highest strain rate,  $\sim 3000 \text{ s}^{-1}$ , the compressive strengths were also found to be comparably smaller than those at lower strain rates. Li and Lambros [33] measured a  $20 \text{ }^\circ\text{C}$  temperature increase during compression testing a carbon reinforced composite along fiber axis at  $3000 \text{ s}^{-1}$ . The lack of the strain rate sensitivity of the tested composite in the through-thickness direction may be due to the specimen heating effect at relatively high strain rates due to adiabatic heating. Much higher stresses and strains experienced by the through-thickness composite specimens than the in-plane specimens until failure favor a higher heating effect in the through-thickness direction. As also cleared from above summary, there exist conflicting results among the studies reported in the literature on the strain rate dependent strength and modulus of CFRPCs. The rate

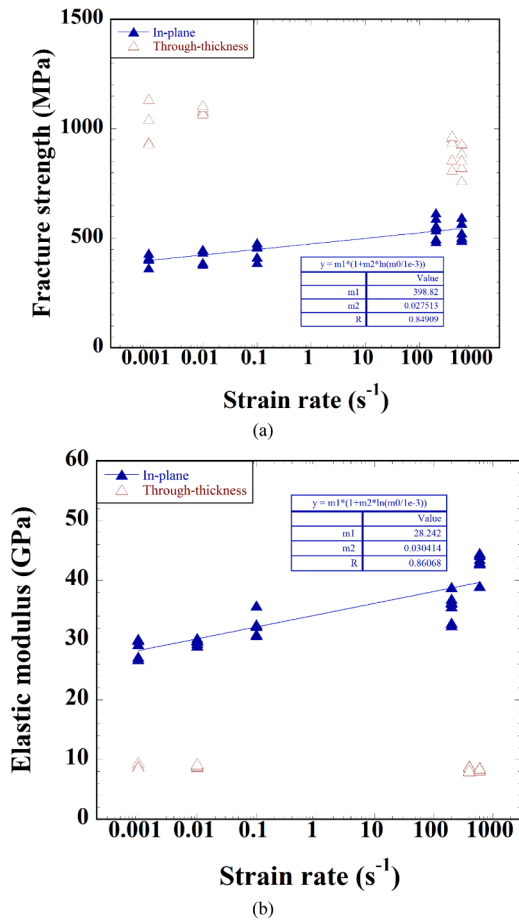


Fig. 9. The variation of (a) fracture strength and (b) elastic modulus of the composite with strain rate in-plane and through-thickness direction.

sensitive strength and modulus in the in-plane direction may also be resulted from the specimen-end effect. The small size specimens may lead to an earlier brooming-dominated failure at the specimen's ends at quasi-static strain rates, while this effect may diminish at high strain rates due to the confining effect of the radial inertia and the strain rate sensitive matrix shear strength. Quasi-static and high strain rate tests were also conducted by confining the ends of the SHPB test specimens using 1 mm-depth end-caps shown in Table 3(7). In these test, although the compressive strength slightly increased with confining, a similar strain rate sensitive strength behavior was also found.

### 5.3. Strain softening property and the modulus reduction parameter

The softening parameters AM1 and AM2 were determined by fitting Eq. (5) with the in-plane SHPB compression stress-strain curves. An example of fitting is shown in Fig. 10(a). The numbers in the same figure correspond to the different values of AM1. When AM1 is zero, the composite shows a linear elastic behavior; while when it is 100, the composite shows a brittle post-failure behavior. A good match is found between the softening behavior of the SHPB in-plane compression stress-strain curve shown in Fig. 10(a) and Eq. (5), when the values of AM1 and AM2 are set to 5.5. Fig. 10(b) shows the experimental (3 tests) and numerical load-time curves of LVI tests. The numerical load values are shown for different values of OMGMX. The initial load-drop seen in the experimental and model load-displacement curves in Fig. 10(b) corresponds to the initiation of a delamination type damage. In the region between initial load-drop and peak-load, a crush type damage occurred by the shearing action of the indenter. The value of AM4 was therefore calibrated with the experimental initial load-drop and the value of AM3

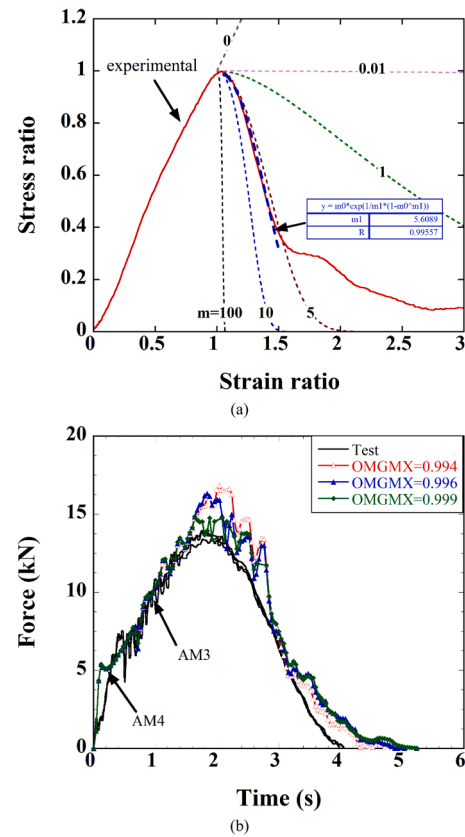


Fig. 10. The fitting (a) AM1 and AM2 with the experimental SHPB tests and (b) AM3, AM4 and OMGMX with the LVI test force time curves.

with the experimental load values between the initial load-drop and peak-load. The fiber damage parameter AM3 and matrix failure and delamination parameter AM4 and OMGMX for glass fiber/epoxy and phenolic matrix composites were reported to vary between 0.1 and 1 and 0.994–0.999, respectively [16]. The best match with the load-time curve in the present study was found when AM3= 0.8 and AM4=0.5. Similarly, a good agreement between the test and model is found when OMGMX value is set to 0.999 as shown in Fig. 10(b). Typical reported values of AM1, AM2, AM3 and AM4 were 2, 2, 0.5 and 0.2 for a PW S2 glass fiber/SC-15 composite [16], 1, 1, 0.5 and 0.2 for a PW E-glass/phenolic composite [11] and 0.6, 0.6, 0.5 and 0.25 for a PW S2-glass/SC-15 epoxy [9] and 4,4,4 and 0.25 for a IM7/8552 composite [1]. Relatively higher values of softening parameters found the tested composite as compared with glass fiber reinforced composites are most likely due to the higher strength and brittleness of the tested composite, leading to higher values of softening parameters. The experimental and numerical maximum displacements of the indenter in the LVI tests are also very similar with each other, sequentially 5.3 and 4.93 mm. Fig. 11 (a) and (b) show the pictures of LVI tested composite plates. Two types experimental damages are seen in the same figures: perpendicular matrix fracture and fiber crush mode. The perpendicular matrix fracture occurs around the indenter-impacted area and seen as lines, while the fiber crush mode occurs at the indenter-impacted region. The numerical models also result in similar damage modes as shown Fig. 11(c) and (d). Fig. 11(c) shows the numerical fiber crush mode and Fig. 11(d) the numerical perpendicular to matrix fracture. The element axial strain, E\_LIMT was determined from the tensile tests in accord with ASTM D3039/D3039M) and the Coulomb friction angle for matrix and delamination (PHIC) was set to 10.



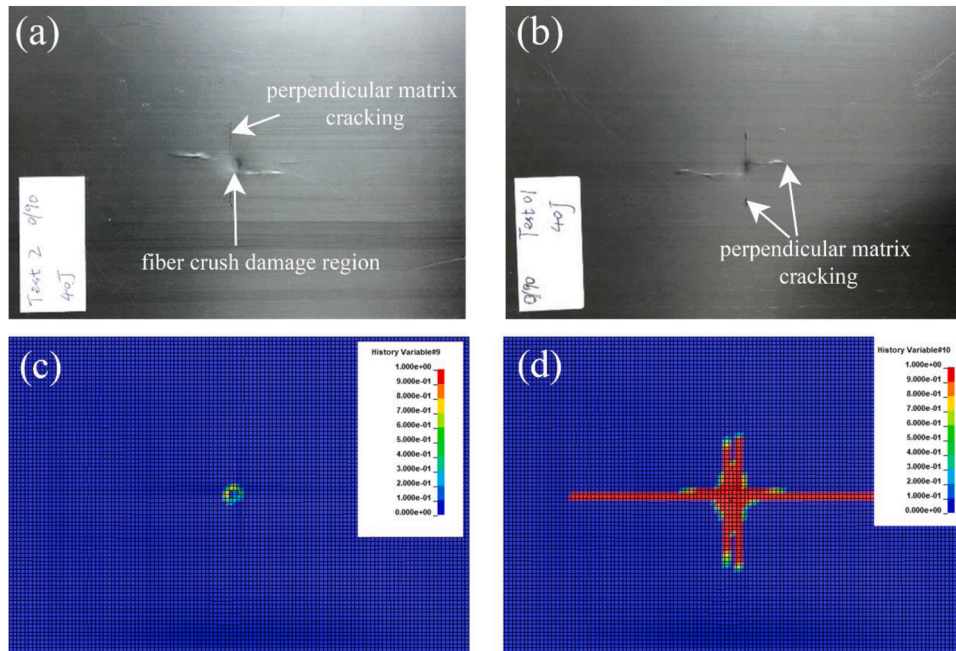


Fig. 11. The pictures of LVI tested specimens (a) showing the fiber crush damage region and (b)perpendicular matrix cracking and numerically tested specimens showing (c) fiber crush mode (failure mode 9) and (d) perpendicular matrix mode (failure mode 10).

5.4. Model verification using SHPB compression tests

The determined MAT\_162 model parameters are tabulated in Table 4 and were used to investigate the progressive failure both in the in-plane and through-thickness direction in the SHPB high strain rate compression test. Fig. 12(a) and (b) show the experimental and numerical reflected and transmitted bar stresses of the composite specimens tested in the in-plane and through-thickness direction, respectively. The initial slower rise of numerical reflected and transmitter bar stresses in the same figures is most likely due to nature of the contacts between the surfaces of specimen and bar in the model and experiments. The contacts in the model are perfect, whereas the contacts in the experiments contain artifacts. Nonetheless, the numerical and experimental stresses show good agreements with each other in the magnitudes of reflected and transmitted stresses as seen in Figs. 12(a) and (b). Fig. 13(a) and (b) show the numerical and experimental deformation histories of the composite specimens tested in the in-plane and through-thickness direction, respectively. The numerical and experimental failures in the in-plane direction initiate by the initiation of local fiber buckling near the bar interfaces as shown by the arrows in Fig. 13(a). The local fiber buckling is followed by the fiber-matrix splitting starting from the incident bar contact. The numerical and experimental failures in the through-thickness direction are matrix shear fracture as marked with the

Table 4  
The determined MAT\_162 material model parameters.

MID	RO	EA	EB	PRAB	PRCA	PRCB
162	1500 (kg m <sup>-3</sup> )	65.1 (GPa)	65.1 (GPa)	0.03	0.054	0.054
GAB	GBC	GCA	SAT	SAC	SBT	SBC
3.61 (GPa)	5.5 (GPa)	5.5 (GPa)	0.736 (GPa)	0.4385 (GPa)	0.736 (GPa)	0.4385 (GPa)
SCT	SFC	SFS	SAB	SBC	SCA	SFFC
0.045 (GPa)	1 (GPa)	0.497 (GPa)	0.055 (GPa)	0.055 (GPa)	0.055 (GPa)	0.3 (GPa)
PHIC	E_LIMT	S_DELM	OMGMX	ECRSH	EEXPXN	CRATE1
10	0.015	1.6	0.999	0.55	1.6	0.028
AM1	AM2	AM3	AM4	CRATE2	CRATE3	CRATE4
5.5	5.5	0.8	0.5	0.03	0.03	0

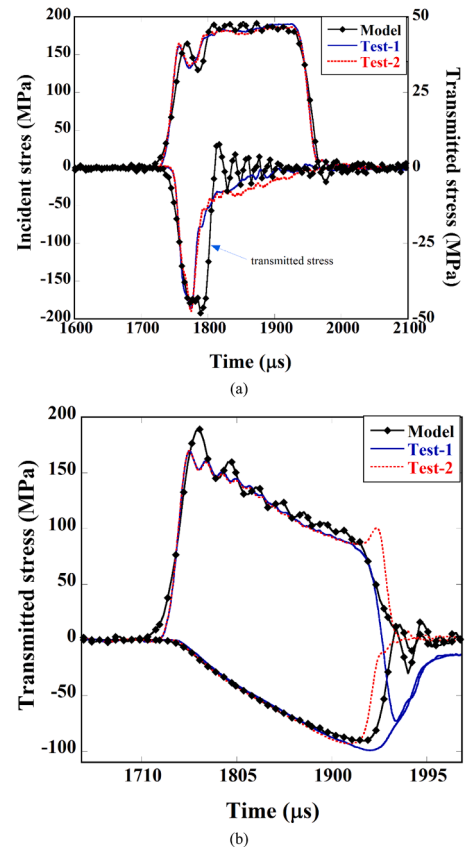
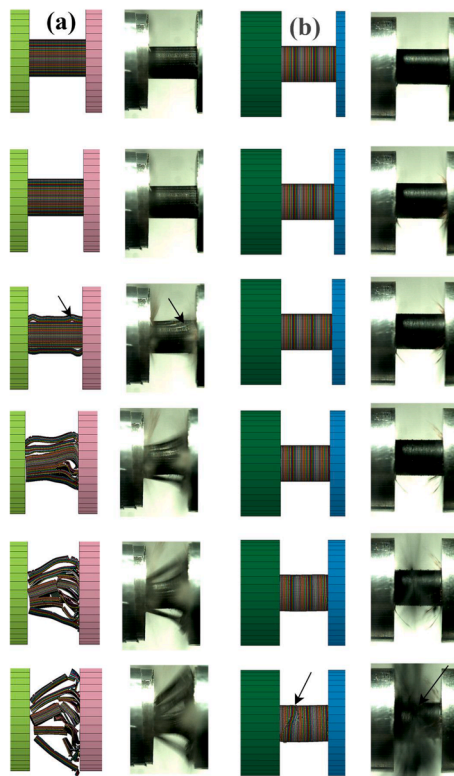


Fig. 12. Stress-time graphs of SHPB tests (a) in-plane and (b) through-thickness direction.

arrows in Fig. 13(b).

Above results confirm the fidelity of the determined material model parameters in predicting the deformation stresses and failure modes of the investigated composite under high strain rate planar compression



**Fig. 13.** Numerical and experimental SHPB compression test progressive damage histories (a) in-plane and (b) through-thickness direction (50 micro-second intervals).

loads. Fine-tuned damage parameters through extensive numerical calibrations may be however needed for the extreme loading cases of non-planar and higher strain rate such as foreign object impact and bird strike. Precise testing methods are also needed to precisely measure the rate sensitive mechanical properties of CFRPCs. The strain rate effect on the stress and the failure modes may play possibly more important roles in the case CFRPC parts are loaded at the strain rates far excess of  $1000 \text{ s}^{-1}$ .

## 6. Conclusions

The dynamic progressive failure of a carbon fiber reinforced laminated ( $0^\circ/90^\circ$ ) epoxy composite was modeled in LSDYNA using the MAT\_162 material model, including strain rate, damage progression and anisotropy effects. The material model parameters of the composite were determined through coupon level tests and the calibrations between model and experiments. In addition to the commonly used test methods, the double-shear and Brazilian tests were applied to determine the through-thickness shear modulus and tensile strength, respectively. The damage and softening parameters were determined by the LVI tests and accompanying numerical model calibration. The fidelity of the developed material model parameters was further verified by the 3D numerical models of the SHPB tests in the in-plane and through-thickness direction at  $600 \text{ s}^{-1}$ . The resulting numerical SHPB bar stresses and the specimen's damage modes well agreed with those of the experiments. The composite failed experimentally and numerically by the local fiber buckling induced fiber-matrix splitting in the in-plane direction and the matrix shear fracture in the through-thickness direction.

## CRediT authorship contribution statement

**Chen Shi:** Data curation, Formal analysis, Visualization. **Baoqiao**

**Guo:** Funding acquisition, Conceptualization, Writing - original draft. **Mustafa Sarıkaya:** Data curation, Validation. **Muhammet Çelik:** Data curation, Validation. **Pengwan Chen:** Project administration, Supervision. **Mustafa Güden:** Investigation, Methodology, Writing - review & editing.

## Declaration of Competing Interest

The authors declare that they have no known competing financial interests or personal relationships that could have appeared to influence the work reported in this paper.

## Acknowledgements

The authors are grateful for financial support from the National Natural Science Foundation of China (Grant No. 11472047). Most of the tests and simulation were performed in the Dynamic Testing and Modeling Laboratory of Izmir Institute of Technology. The first author Chen Shi would greatly acknowledge Professor Mustafa Güden for his hosting and supervision.

## Supplementary materials

Supplementary material associated with this article can be found, in the online version, at doi:10.1016/j.ijimpeng.2020.103771.

## References

- [1] Maio L, et al. Simulation of low velocity impact on composite laminates with progressive failure analysis. *Compos Struct* 2013;103(0):75–85.
- [2] Qu P, et al. A new numerical model for the analysis on low-velocity impact damage evolution of carbon fiber reinforced resin composites. *J Appl Polym Sci* 2017;134(4):9.
- [3] Farooq U, Myler P. Efficient computational modelling of carbon fibre reinforced laminated composite panels subjected to low velocity drop-weight impact. *Mater Des* 2014;54:43–56.
- [4] Chang F-K, Chang K-Y. A progressive damage model for laminated composites containing stress concentrations. *J Compos Mater* 1987;21(9):834–55.
- [5] LSTC, *ls-dyna keyword user's manual vol. ii*. Livermore Software Technology Corporation (LSTC); 2007.
- [6] Hashin Z. Failure criteria for unidirectional fiber composites. *J Appl Mech* 1980;47(2):329–34.
- [7] Matzenmiller A, Lubliner J, Taylor RL. A constitutive model for anisotropic damage in fiber-composites. *Mech Mater* 1995;20(2):125–52.
- [8] Xiao JR, Gama BA, Gillespie Jr JW. Progressive damage and delamination in plain weave S-2 glass/SC-15 composites under quasi-static punch-shear loading. *Compos Struct* 2007;78(2):182–96.
- [9] Deka LJ, Bartus SD, Vaidya UK. Damage evolution and energy absorption of E-glass/polypropylene laminates subjected to ballistic impact. *J Mater Sci* 2008;43(13):4399–410.
- [10] Gama BA, Gillespie JW. Finite element modeling of impact, damage evolution and penetration of thick-section composites. *Int J Impact Eng* 2011;38(4):181–97.
- [11] Jordan JB, Naito CJ, Haque BZ. Progressive damage modeling of plain weave E-glass/phenolic composites. *Compos Part B* 2014;61(0):315–23.
- [12] Tasdemirci A, et al. Experimental and numerical investigation of high strain rate mechanical behavior of a [0/45/90/- 45] quadriaxial E-glass/polyester composite. *Procedia Eng* 2011;10(0):3068–73.
- [13] Odaci IK. Experimental and numerical evaluation of the blast-like loading of fiber reinforced polymer composites and aluminum corrugated core composite sandwiches through projectile impact testing using aluminum corrugated projectiles. *Mechanical engineering*. Izmir: Izmir Institute of Technology; 2015.
- [14] Hazzard MK, et al. Finite element modelling of Dyneema® composites: from quasi-static rates to ballistic impact. *Compos Part A* 2018;115:31–45.
- [15] Molitor M, et al. Comparison of test methods to determine failure parameters for MAT162 calibration. In: 2018 AIAA/ASCE/AHS/ASC structures, structural dynamics, and materials conference; 2018.
- [16] Gama BZ. A progressive composite damage model for unidirectional and woven fabric composites-UD-CCM updates on MAT162 user manual version 17A-2017. University of Delaware Center for Composite Materials; 2017.
- [17] Gama BA, Lopatnikov SL, Gillespie JJW. Hopkinson bar experimental technique: a critical review. *Appl Mech Rev* 2004;57(4):223–50.
- [18] Mishra S, et al. High strain rate response of rocks under dynamic loading using split hopkinson pressure bar. *Geotech Geol Eng* 2018;36(1):531–49.
- [19] Kolsky H. An investigation of the mechanical properties of materials at very high rates of loading. *Proc Phys Soc Section B* 1949;62(11):676.
- [20] Davies EDH, Hunter SC. The dynamic compression testing of solids by the method of the split Hopkinson pressure bar. *J Mech Phys Solids* 1963;11(3):155–79.

- [21] Ravichandran G, Subhash G. Critical-appraisal of limiting strain rates for compression testing of ceramics in a split hopkinson pressure bar. *J Am Ceram Soc* 1994;77(1):263–7.
- [22] Hall IW, Guden M. High strain rate testing of a unidirectionally reinforced graphite epoxy composite. *J Mater Sci Lett* 2001;20(10):897–9.
- [23] Sivashanker S, Osiyemi SO, Bag A. Compressive failure of a unidirectional carbon-epoxy composite at high strain rates. *Metall Mater Trans a-Phys Metall Mater Sci* 2003;34A(6):1396–400.
- [24] Gillespie JW, et al. Interlaminar shear strength of plain weave S2-glass/SC79 composites subjected to out-of-plane high strain rate compressive loadings. *Compos Sci Technol* 2005;65(11–12):1891–908.
- [25] Yokoyama T. Impact compressive failure of a unidirectional carbon/epoxy laminated composite in three principal material directions. In: Chandra T, Ionescu M, Mantovani D, editors. *Thermec 2011, Pts 1-4*. Stafa-Zurich: Trans Tech Publications Ltd; 2012. p. 799–804.
- [26] Gama BA, Gillespie JW. Punch shear based penetration model of ballistic impact of thick-section composites. *Compos Struct* 2008;86(4):356–69.
- [27] Chen X, et al. The compressive and tensile behavior of a 0/90 C fiber woven composite at high strain rates. *Carbon N Y* 2013;61(0):97–104.
- [28] Lui JH, et al. Experimental study of in-plane mechanical properties of carbon fibre woven composite at different strain rates. *Polym Polym Compos* 2017;25(4):289–98.
- [29] Ashby MF, et al. Chapter 4 - properties of metal foams. In: Ashby MF, et al., editors. *Metal foams*. Burlington: Butterworth-Heinemann; 2000. p. 40–54.
- [30] Kwon J, et al. Evaluation of the effect of the strain rate on the tensile properties of carbon–epoxy composite laminates. *J Compos Mater* 2016;51(22):3197–210.
- [31] Hosur MV, et al. High strain compression response of affordable woven carbon/epoxy composites. *J Reinf Plast Compos* 2003;22(3):271–96.
- [32] Naik NK, Kavala VR. High strain rate behavior of woven fabric composites under compressive loading. *Mater Sci Eng a-Struct Mater Prop Microstruct Process* 2008;474(1–2):301–11.
- [33] Li Z, Lambros J. Dynamic thermomechanical behavior of fiber reinforced composites. *Compos Part A* 2000;31(6):537–47.